GEOPHYSICS, VOL. 67, NO. 6 (NOVEMBER-DECEMBER 2002); P. 1740–1752, 7 FIGS., 2 TABLES.
10.1190/1.1527075

Time-lapse inversion of crosswell radar data

Frederick D. Day-Lewis*, Jerry M. Harris‡, and Steven M. Gorelick**

ABSTRACT

The combination of differential radar tomography with conventional tracer and/or hydraulic tests facilitates high-resolution characterization of subsurface heterogeneity and enables the identification of preferential flow paths. In dynamic imaging, each tomogram is typically inverted independently, under the assumption that data sets are collected quickly relative to changes in the imaged property (e.g., attenuation or velocity); however, such "snapshot" tomograms may contain large errors if the imaged property changes significantly during data collection. Acquisition of less data over a shorter time interval could ameliorate the problem, but the resulting decrease in ray density and angular coverage could degrade model resolution. To address these problems, we propose a new sequential approach for time-lapse tomographic inversion. The method uses space-time parameterization and regularization to combine data collected at multiple times and to account for temporal variation. The inverse algorithm minimizes the sum of weighted squared residuals and a measure of solution complexity based on an a priori space-time covariance function and a spatiotemporally variable mean. We demonstrate our approach using a synthetic 2-D time-lapse (x, z, t) data set based loosely on a field experiment in which difference-attenuation radar tomography was used to monitor the migration of a saline tracer in fractured rock. We quantitatively show the benefits of space-time inversion by comparing results for snapshot and time-lapse inversion schemes. Inversion over both space and time results in superior estimation error, model resolution, and data reproduction compared to conventional snapshot inversion. Finally, we suggest strategies to improve time-lapse cross-hole inversions using ray-based inversion constraints and a modified survey design in which different sets of rays are collected in alternating time steps.

INTRODUCTION

Accurate and reliable characterization of aquifer heterogeneity remains one of the foremost problems in hydrogeology. Traditional hydrogeologic measurements are sparse and sample poorly defined aquifer volumes limited to the vicinity of boreholes. Near-surface geophysical exploration methods can provide additional information about hydrogeologic properties between or away from boreholes (e.g., Rubin et al., 1992; Copty et al., 1993; Hyndman et al., 1994, 2000; Hyndman and Gorelick, 1996; Hyndman and Harris, 1996; Poeter et al., 1997; Ezzedine et al., 1999; Hubbard et al., 1999, 2001); however, the relationship between geophysical properties and hydraulic conductivity is complex, nonunique (Marion et al., 1992; Hyndman et al., 1994), and scale dependent (Hyndman et al., 2000). One solution is to use "differential geophysics" to monitor changes concomitant with engineering stress tests, contaminant migration, or natural physical processes (e.g., White, 1988; Brewster and Annan, 1994; Brewster et al., 1995; Osiensky and Donaldson, 1995; Ramirez et al., 1996; Slater and Sandberg, 2000; Slater et al., 2000; Hubbard et al., 2001). Measurements are collected before, perhaps during, and after an imposed change to the system. Inverted difference images reveal changes that vary over space and time and can be related to hydrogeologic features, such as fractures containing high solute concentrations. We believe the combination of dynamic geophysical imaging with traditional hydrologic testing holds great promise for improving aquifer characterization.

Of particular use in near-surface settings is ground-penetrating radar (GPR), which may offer submeter resolution. Radar velocity and attenuation are sensitive to contrasts in several properties of hydrologic relevance. Radar

Manuscript received by the Editor January 24, 2001; revised manuscript received March 1, 2002.
*Bucknell University, Department of Geology, Lewisburg, Pennsylvania 17837. E-mail: fdaylewi@bucknell.edu.
‡Stanford University, Department of Geophysics, Stanford, California 94305. E-mail: harris@geo.stanford.edu.
**Stanford University, Department of Geological and Environmental Sciences, Stanford, California 94305. E-mail: gorelick@geo.stanford.edu.

attenuation tomography yields images (tomograms) of variations in electrical conductivity, which is a function of pore-fluid salinity. Velocity tomography maps variations in dielectric permittivity, which is a function of water content and porosity. In the landmark Stripa mine fractured rock study, Olsson et al. (1992) used radar methods to identify and delineate fracture zones; Olsson et al. (1991) collected radar amplitude data during a saline tracer test and inverted for three difference-attenuation tomograms. Radar tomography has also been used in conjunction with tracer tests at the U.S. Geological Survey Fractured Rock Hydrology Research Site near Mirror Lake, New Hampshire (Lane et al., 1998, 2000). Lane et al. (1998) developed a novel sequential-injection and scanning method to collect time-lapse data during saline tracer tests. Eppstein and Dougherty (1998a) monitored changes in soil moisture during fluid injection in the vadose zone using cross-borehole GPR.

Difference tomograms are typically generated based on a single time-lapse data set. If multiple tomograms are computed, they are inverted independently (e.g., Olsson et al., 1991; Eppstein and Dougherty, 1998a; Lane et al., 1998, 2000; Hubbard et al., 2001). These studies relied on the assumption that data used to invert each tomogram were collected over a sufficiently short period of time that changes in the imaged property during data collection were negligible. If, however, the tracer concentration or distribution changes quickly over the data collection period, this assumption could result in poor data reproduction and errors in tomograms.

We propose space-time inversion as a means to overcome this limitation and account for, indeed, to take advantage of space-time parameter correlation and precise data-acquisition times. Using data collected at multiple times should improve the signal-to-noise ratio and model resolution. Our space-time tomographic inverse approach is applied to a synthetic example, and we assess its advantages over independent "snapshot" inversion methods in terms of estimation error, model resolution, and data reproduction. The synthetic example is based loosely on a field experiment at the U.S. Geological Survey Fractured Rock Hydrology Research Site, in which difference-attenuation tomography was used to monitor tracer migration during a series of saline tracer tests (Lane et al., 2000).

The time-lapse inversion combines data from multiple times, thereby exploiting temporal correlation. The forward model accounts for measurement collection time, and a nodal parameterization allows for the physical properties to vary smoothly in space and time. At each step of the inversion, nodal parameters (i.e., difference attenuation in this study) in a temporal window are updated using all measurements collected inside the window. The window advances in time as the inversion proceeds. The inversion algorithm minimizes a combination of (1) the sum of weighted squared data residuals and (2) a measure of solution complexity based on an a priori space-time covariance function. Additionally, we consider strategies to enhance model resolution including (1) a modified survey design in which different source-receiver geometries are used in alternating time steps, (2) use of additional time-sets of data in each time-lapse inversion step, and (3) application of ray-based inversion constraints to restrict attenuation anomalies to regions of the tomograms traversed by high difference-amplitude raypaths.

BACKGROUND

Radar wave propagation

In radar tomography (e.g., Olsson et al., 1991, 1992; Eppstein and Dougherty, 1998a; Lane et al., 1998; Holliger et al., 2001; Peterson, 2001) electromagnetic waves are transmitted from transmitter-antenna locations in one borehole to receiver-antenna locations in one or more boreholes where waveform data are collected. Typical center frequencies vary from 20 to 200 MHz. Quantities such as traveltime, energy, or amplitude are calculated for each waveform trace. Processed data are inverted to yield images of velocity, attenuation, or other quantities in the image planes. In GPR studies, it is typically assumed that wave propagation dominates over conduction. Under this assumption, radar velocity is a function of magnetic permeability and dielectric constant, whereas radar attenuation is a function of these properties as well as electrical conductivity (Stratton, 1941, 275–277), which increases with salinity (Archie, 1942).

In problems where velocity contrasts are significant, ray bending occurs according to Snell's law, and the tomographic inversion is nonlinear. This is typical in seismic applications, where velocity variations can be large. In radar tomography, the straight-ray assumption is often reasonable, as radar velocity in the near subsurface tends not to be highly variable. Furthermore, because radar velocity is only a weak function of salinity, ray bending due to salinity changes can often be ignored.

Difference-attenuation tomography

In attenuation tomography, the peak amplitude is measured for a number of raypaths between transmitter positions in one borehole and receiver positions in a second borehole. Inversion of amplitude data generates tomograms of attenuation. Assuming straight rays, amplitude decay is a function of distance from the transmitter, the attenuation of the medium, and the antenna radiation patterns (e.g., Holliger et al., 2001):

$$A(r) \propto \frac{A_0 \exp(-\alpha(r))\Theta_T(\varphi)\Theta_R(\varphi)}{r}, \qquad (1)$$

where $A(r)$ is the peak amplitude of the measured trace at distance r from the transmitter, A_0 is a normalization factor combining the effects of antenna gain and efficiency, α is the attenuation of the medium, Θ_T is the radiation pattern of the transmitter antenna, Θ_R is the radiation pattern of the receiver antenna, and φ is the angle of the ray with respect to horizontal. Thus, trace amplitude is an integrated measurement of attenuation along the raypath between the transmitter and receiver locations. The problem (1) is linearized by taking logarithms, and then discretized over the tomogram, which is typically parameterized as a pixelated grid. This results in a linear system of equations relating measurements (amplitudes) to model parameters (e.g., pixel attenuations):

$$-\ln \frac{A_i r}{\Theta_T(\varphi)\Theta_R(\varphi)} = -\ln A_0 + \sum_j \alpha_j \ell_{ij}, \qquad (2)$$

where A_i is the amplitude of ray i, α_j is the attenuation in pixel j, and ℓ_{ij} is the distance traveled by the ray i in pixel j. Inversion of equation (2) to estimate absolute attenuation, α,

requires assumption of a model for the unknown antenna radiation (Holliger et al., 2001; Peterson, 2001). Fortunately, reliance on these models is reduced in the estimation of difference attenuation, $\Delta\alpha$, from difference-amplitude data.

There are two approaches to difference-attenuation tomography. The first involves inversion of two sets of amplitude data to yield two attenuation tomograms, which are subsequently differenced. The second approach inverts ray "difference-amplitude data" to directly produce difference-attenuation tomograms. This is achieved by calculating the difference between two amplitude data sets: A^k, collected at time k, and A^0, a background data set collected before an imposed change to the system (e.g., tracer injection). If we again assume straight rays and further assume that antenna-radiation patterns are constant in time, then

$$\ln \frac{A_i^0}{A_i^k} = \sum_{j=1}^{npixels} \Delta\alpha_j^k r_{ij}, \tag{3}$$

where $\Delta\alpha_j^k$ is the difference attenuation at time k in pixel j, $\Delta\alpha_j^k = \alpha_j^k - \alpha_j^0$, *npixels* is the number of pixels, α_j^k is the attenuation at time k in pixel j, and α_j^0 is the attenuation in pixel j at the reference time, before the imposed change. Inversion of difference-amplitude data [the left-hand side of equation (3)] obviates the requirement to know the antenna-radiation patterns. Moreover, examination of difference data yields valuable insight into the spatial distribution of tracer during geophysical monitoring. Such insight provides a basis for the development of ray-based constraints on estimates of difference attenuation. For these reasons, we work with difference-amplitude data in this study.

Experimental time-lapse data collection

In time-lapse cross-borehole seismic or resistivity surveys, multiple receivers and/or sources are used. When a source is triggered, many receivers simultaneously collect measurements. Thus, a common-source gather is collected instantaneously, and a survey, comprising a number of gathers, can be collected in a short span of time without having to relocate sources or receivers for each measurement. This is not the case with present borehole-radar systems. Most commercially available borehole-radar systems employ one transmitter antenna and one receiver antenna, thus hindering rapid time-lapse data collection. A radar antenna must be moved for each measurement. Thus, each measurement in a gather, and each gather in a survey, is collected at a different time. This results in an unfortunate tradeoff between (1) obtaining sufficient raypath coverage in each survey, and (2) minimizing the time interval over which a survey is collected, so that temporal changes in the physical properties of the subsurface are negligible. The quality of the inversion will suffer if spatial coverage is poor or if data are inconsistent due to neglected temporal changes. One strategy is to reduce injection and pumping rates to minimize concentration changes during data collection steps. However, tracer-test design is commonly dictated by hydrogeologic rather than geophysical considerations. At high flow velocities, advection dominates and preferential flowpaths are best illuminated. Furthermore, density-driven flow due to high-concentration saline tracers will be minimized under higher flow rates, facilitating tracer-test interpretation using standard models. A second, more attractive strategy is to employ space-time parameterization and inverse modeling to account for staggered acquisition times and space-time correlation of tracer concentration.

Tomographic inversion

Tomographic inversion typically involves the solution of large (many thousands of data and estimated parameters) underdetermined or mixed-determined systems of equations. In mixed-determined systems, data are sufficient to resolve some, but not all, parameters (e.g., pixel difference-attenuation values). Inversion requires the addition of prior information, usually in the form of minimum-length or smoothness criteria (Menke, 1989). Large problems often require iterative row-action solvers such as ART or SIRT (Censor, 1983; Peterson et al., 1985) instead of optimal least-squares approaches that employ matrix decomposition or inversion. Inverse solutions may be contaminated by data errors and may exhibit artifacts due to poor model resolution. Numerous approaches and strategies to problems of model parameterization and inversion are found in the literature. Some recent advances include the application of the extended Kalman filter to sequentially incorporate data for optimal estimation (Eppstein and Dougherty, 1998b), methods to constrain tomograms to include a small number of homogenous zones (Hyndman et al., 1994; Hyndman and Harris, 1996; Eppstein and Dougherty, 1998b), inversion on staggered and adapted grids (Vesnaver and Böhm, 1999, 2000), and the use of stochastic regularization to cope with model ambiguity for large, underdetermined problems (Maurer et al., 1998). Other strategies include the application of ray-based constraints to limit anomalies to certain regions of the tomogram (Singh and Singh, 1991), and parameterization linked to the underlying physics of wave propagation (Michelena and Harris, 1991).

TIME-LAPSE INVERSION METHODOLOGY

Space-time parameterization

The forward model for calculating difference-amplitude data requires parameterization of difference attenuation in the interwell region. Commonly, the tomogram is discretized as a regular grid of square pixels. We instead employ a space-time nodal mesh and interpolate difference-attenuation between nodes for ray-tracing and display purposes. The nodal parameterization allows difference attenuation to vary smoothly in space and time, whereas pixels are assumed homogeneous. Moreover, a mesh is better suited to space-time interpolation than is a pixelated grid, and is easily adapted for problems with deviated wells or multiple image planes. In the following synthetic example, the image domain is discretized into a 3-D $(\mathbf{x}, t)$ mesh of 8-node linear-brick elements. The 3-D space-time mesh can be thought of as a time series of identical 2-D spatial meshes. To construct the 2-D spatial mesh, we use a constant vertical spacing between *nz* layers of nodes, with a set number of nodes *nr* in each layer.

Difference attenuation at particular position and time, $\Delta\alpha(\mathbf{x}, t)$, is interpolated as a weighted average of nodal difference-attenuation values, with the weights specified by Lagrange interpolation functions for cubic-quadrilateral finite

elements (Istok, 1989, 109; and our Appendix A):

$$\Delta\alpha(\mathbf{x}, t) = \sum_{k=1}^{ntimes} \sum_{j=1}^{nnodes} w_j^k(\mathbf{x}, t)\Delta\alpha_j^k, \quad (4)$$

where $w_j^k(\mathbf{x}, t)$ is the Lagrange interpolation function at spatial location $(\mathbf{x}, y)$ and time t for node j at mesh-time T^k, *ntimes* is the number of time mesh times, *nnodes* is the number of nodes in each 3-D mesh, and $\Delta\alpha_j^k$ is the difference attenuation of node j in the T^k-time mesh.

Forward model

We model the difference amplitude at a receiver as the line integral of difference attenuation along the raypath. To account for temporal variation during data acquisition, the forward model for a data set depends on difference attenuation (expressed in decibels/meter) in two temporally adjacent 2-D (x, z) meshes:

$$d_i^k = 20\log_{10}\frac{A_i^0}{A_i^k} = \int_{R_i} \Delta\alpha(\mathbf{r}, t_i^k)\, d\mathbf{r} \approx \sum_{j=1}^{nnodes} G_{ij}^{k,k}\Delta\alpha_j^k + \sum_{j=1}^{nnodes} G_{ij}^{k,k+1}\Delta\alpha_j^{k+1}, \quad (5)$$

where d_i^k is the simulated difference-amplitude for ray i in the k-time data set (expressed in decibels), $\mathbf{r}$ is the point in space along the raypath R_i, t_i^k is the collection time for ray i in the k-time data set (in minutes since the start of injection), and $G_{ij}^{k,\ell}$ is the influence of node j in the T^ℓ-time mesh on ray i in the k-time data set (in meters).

Constructing the raypath matrix, $\mathbf{G}$, for a 2-D pixelated grid would require calculation of the lengths traveled by each ray in each pixel. For the space-time nodal mesh, we must determine the length of each ray attributed to each node, in both space and time. The effect of node j in the T^ℓ-mesh on ray i collected in the k-data set is calculated as the nodal interpolation function integrated numerically along the ray path R_i:

$$G_{ij}^{k,\ell} = \int_{R_i} w_j^\ell(\mathbf{r}, t_i^k)\, d\mathbf{r} \approx \sum_{m=1}^{nsteps} w_j^\ell(\mathbf{x}_s + (m-1/2)\Delta\mathbf{x}, t_i^k)\|\Delta\mathbf{x}\|, \quad (6)$$

where *nsteps* is the number of increments from the source location $\mathbf{x}_S$ to the receiver location $\mathbf{x}_R$, and $\Delta\mathbf{x}$ is the increment vector $(\mathbf{x}_R - \mathbf{x}_S)/nsteps$.

Tomographic inverse method

To use all data to estimate all parameters simultaneously would be computationally intractable for most time-lapse tomographic problems. Inversion for static phenomena can involve thousands or tens of thousands of data and estimated parameters. In dynamic imaging, the number of parameters and unknowns grows according to the number of time-lapse tomograms and data sets. To overcome this problem, we apply sequential inversion, using N time-sets of data to estimate the $N+1$ time-sets of parameters of which they are functions (Figure 1). For example, the forward model $\boldsymbol{\delta}^k = \boldsymbol{\Gamma}^k\,\mathbf{m}^k$ for $N=2$ is

$$\begin{bmatrix}\mathbf{d}^{k-1}\\ \mathbf{d}^k\end{bmatrix} = \begin{bmatrix}\mathbf{G}^{k-1,k-1} & \mathbf{G}^{k-1,k} & \mathbf{0}\\ \mathbf{0} & \mathbf{G}^{k,k} & \mathbf{G}^{k,k+1}\end{bmatrix}\begin{bmatrix}\boldsymbol{\Delta\alpha}^{k-1}\\ \boldsymbol{\Delta\alpha}^k\\ \boldsymbol{\Delta\alpha}^{k+1}\end{bmatrix}. \quad (7)$$

Each tomographic inversion step seeks to minimize Z, a combination of the sum of weighted squared data residuals and a measure of solution complexity based on an a priori covariance model:

$$Z = (\boldsymbol{\delta}^k - \boldsymbol{\Gamma}^k\hat{\mathbf{m}}^k)^T\mathbf{V}^{-1}(\boldsymbol{\delta}^k - \boldsymbol{\Gamma}^k\hat{\mathbf{m}}^k) + (\hat{\mathbf{m}}^k - \mathbf{X}\boldsymbol{\beta})^k\mathbf{Q}^{-1}(\hat{\mathbf{m}}^k - \mathbf{X}\boldsymbol{\beta}),\ k = 1, nsteps, \quad (8)$$

where $\boldsymbol{\delta}^k$ is the data vector containing N time-sets of data for step k of the inversion; $\boldsymbol{\Gamma}^k$ is the data kernel for step k of the inversion, corresponding to N time-sets of data and $N+1$ time-meshes of nodes; $\hat{\mathbf{m}}^k$ is the vector of model parameter estimates for $N+1$ time-meshes of nodes in step k of the inversion; $\mathbf{V}$ is a diagonal matrix with elements equal to the error variances of $\boldsymbol{\delta}$; $\mathbf{Q}$ is the prior covariance matrix for model parameters $\hat{\mathbf{m}}^k$; $\mathbf{X}$ is a matrix defining the form of the spatiotemporal mean (e.g., a constant or linear trend), and $\boldsymbol{\beta}$ are the mean values determined by the inversion. The index k is incremented as the inversion proceeds. Each step in the inversion produces estimates of difference-attenuation at $N+1$ times, and difference-attenuation at each time is estimated in $N+1$ steps. The final estimate is taken from the step in which those parameters are best resolved. For example, in the case of $N=2$, each k-set of difference-attenuation values would be estimated three times: using first the $k-2$ and $k-1$ data sets, then the $k-1$ and k sets, and finally the k and $k+1$ sets. The final estimate vector for time k would be the one based on the $k-1$ and k data sets because this estimation was based on the most informative data for time k (Figure 1). Alternatively, the different estimates could be averaged to produce increased temporal smoothness, much as spatial smoothing filters are sometimes applied to tomograms as a postprocessing step (e.g., Hyndman et al., 1994). However, any resulting aesthetic improvement would likely increase the model response misfit to the data.

The mean, $\mathbf{X}\boldsymbol{\beta}$, can be defined to account for spatial and/or temporal trends. Numerous forms are possible, including linear or polynomial spatiotemporal trends or homogeneous zones. The form, $\mathbf{X}$, of the mean is defined a priori, but the mean values, $\boldsymbol{\beta}$, are found by the inversion. Note that temporal changes in the mean values are partly accounted for by the sequential estimation, which allows the mean values to change through time. The parameter vector $\hat{\mathbf{m}}^k$ that minimizes equation (8) is found by solving

$$\left(\boldsymbol{\Gamma}^{k^T}\mathbf{V}^{-1}\boldsymbol{\Gamma}^k + \mathbf{M}\right)\hat{\mathbf{m}}^k = \boldsymbol{\Gamma}^{k^T}\mathbf{V}^{-1}\boldsymbol{\delta}^k, \quad (9)$$

where

$$\mathbf{M} = \mathbf{Q}^{-1} - \mathbf{Q}^{-1}\mathbf{X}(\mathbf{X}^T\mathbf{Q}^{-1}\mathbf{X})^{-1}\mathbf{X}^T\mathbf{Q}^{-1}. \quad (10)$$

The minimization (9) is based on the estimation step in the "geostatistical approach" used for hydrogeologic parameter estimation with a spatially variable mean (e.g., Kitanidis and Vomvoris, 1983; Kitanidis, 1995, 1996).

A number of spatiotemporal covariance models are found in the literature (Kyriakidis, 1999). We model the space-time covariance as the product of separable spatial and temporal

spherical covariance functions (e.g., Rouhani and Myers, 1990):

$$Q(h,\tau) = Q_o\rho_x(h)\rho_t(\tau) = Q_o\left[1-\left(\frac{3}{2}h-\frac{1}{2}h^3\right)\right] \times\left[1-\left(\frac{3}{2}\tau-\frac{1}{2}\tau^3\right)\right], \quad (11)$$

if $h < a_x$ and $\tau < a_t$, or 0 otherwise, where $Q(h,\tau)$ is the space-time covariance, $\rho_x(h)$ and $\rho_t(\tau)$ are the spatial and temporal correlation functions, respectively, Q_o is the variance, h is the spatial separation distance, τ is the temporal separation, a_x is the spatial correlation range, and a_t is the temporal correlation range.

In some problems, attenuation changes may be confined to a small region of the tomogram. For example, tracer transport in fractured rock is typically focused in a few permeable fractures; thus, only a small population of rays will traverse the anomaly. However, if the inverse problem is severely underdetermined (as is usually the case), the anomaly may artificially blur or smear outside this region. In such cases, the use of ray-based constraints can improve model resolution. For example, Lane et al. (1998) used the iterative ray-projection technique algorithm (Singh and Singh, 1991) to restrict difference-attenuation anomalies to regions traversed by high difference-amplitude raypaths. To facilitate calculation of the model and data resolution matrices for constrained inversion, we instead impose zero-value, ray-based constraints using Lagrange multipliers. The solution for the constrained problem, $\hat{\mathbf{m}}^{k'}$, is determined by solving the linear system

$$\begin{bmatrix}\boldsymbol{\Gamma}^{k^T}\mathbf{V}^{-1}\boldsymbol{\Gamma}^k+\mathbf{M} & \mathbf{F}^T\\ \mathbf{F} & \mathbf{0}\end{bmatrix}\begin{bmatrix}\hat{\mathbf{m}}^{k'}\\ \boldsymbol{\lambda}\end{bmatrix}=\begin{bmatrix}\boldsymbol{\Gamma}^{k^T}\mathbf{V}^{-1}\boldsymbol{\delta}^k\\ \mathbf{0}\end{bmatrix}, \quad (12)$$

where $\mathbf{F}\hat{\mathbf{m}}^{k'}=\mathbf{0}$ are the nodal constraints, and $\boldsymbol{\lambda}$ is the vector of Lagrange multipliers.

It is generally more efficient to solve the linear systems (9) or (12) using LU decomposition and then backsolving rather than to attempt full matrix inversion to calculate the estimates directly. However, to compute model resolution matrices requires that we define the approximate inverses for the constrained and unconstrained problems ($\boldsymbol{\Gamma}^{k\dagger}$ and $\boldsymbol{\Gamma}^{k\dagger'}$, respectively) such that $\hat{\mathbf{m}}^k=\boldsymbol{\Gamma}^{k\dagger}\boldsymbol{\delta}^k$ and $\hat{\mathbf{m}}^{k'}=\boldsymbol{\Gamma}^{k\dagger'}\boldsymbol{\delta}^k$:

$$\boldsymbol{\Gamma}^{k\dagger}=\left(\boldsymbol{\Gamma}^{k^T}\mathbf{V}^{-1}\boldsymbol{\Gamma}^k+\mathbf{M}\right)^{-1}\boldsymbol{\Gamma}^{k^T}\mathbf{V}^{-1}, \quad (13)$$

$$\Gamma^{k\dagger'}=\left\{\mathbf{I}-\left(\boldsymbol{\Gamma}^{k^T}\mathbf{V}^{-1}\boldsymbol{\Gamma}^k+\mathbf{M}\right)^{-1}\mathbf{F}^T\left[\mathbf{F}\left(\boldsymbol{\Gamma}^{k^T}\mathbf{V}^{-1}\boldsymbol{\Gamma}^k+\mathbf{M}\right)^{-1}\mathbf{F}^T\right]^{-1}\mathbf{F}\right\}\boldsymbol{\Gamma}^{k\dagger}. \quad (14)$$

The sequential approach described here facilitates the calculation of resolution matrices and is computationally efficient.

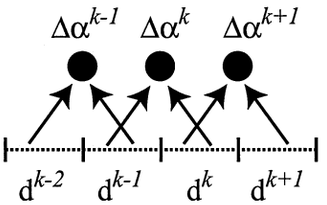

FIG. 1. Data stencil used to estimate nodal parameters at different times for $N=2$. Data sets $k-1$ and k are used to estimate each k set of parameters.

Our technique does not require repeated matrix inversions or covariance updating, because we use the same approximate inverse for multiple time steps under the assumption of a static covariance model. For example, if the same data configuration was used for every time step, then the same forward and inverse models are used in every time step. The sequential inversion would therefore require a single LU decomposition for one approximate inverse and then backsolving for different right-hand sides at each step.

Model resolution

The model resolution matrix, $\mathbf{R}$, is useful for quantifying the nonuniqueness of inversion results in underdetermined problems (Menke, 1989). $\mathbf{R}$ can be thought of as the lens or filter through which the inversion sees the earth, taking into account the forward model, the source-receiver acquisition geometry, the weights on the data, and any a priori information we choose to apply. Row i of $\mathbf{R}$ describes the resolution of model parameter i (difference attenuation at node i). If parameter i is resolved uniquely, R_{ii} is one, and all other elements of row i are zero. If R_{ii} is zero, parameter i can not be resolved by the data. A nonzero off-diagonal element R_{ij} indicates that the estimation of parameter i is affected by parameter j. For a purely overdetermined problem, all model parameters can be resolved, and $\mathbf{R}$ is an identity matrix. $\mathbf{R}$ can be used to forward model, or predict, the result of an inversion, $\hat{\mathbf{m}}$, for a given data configuration and hypothetical model $\mathbf{m}$; i.e., $\hat{\mathbf{m}}=\mathbf{R}\,\mathbf{m}$. Thus, the resolution matrix can be used to evaluate the effect of different sampling schemes (in space and time), parameterizations, constraints, and regularization methods on the inversion results. Typically, $\mathbf{R}$ is computed for the case of the natural, generalized inverse using singular-value decomposition of the data kernel. However, $\mathbf{R}$ can be computed for alternative inverse models if $\boldsymbol{\Gamma}^{\dagger}$ is available (Vasco et al., 1997). In this case, $\mathbf{R}$ is equal to $\boldsymbol{\Gamma}^{\dagger}\boldsymbol{\Gamma}$. The resolution matrix for a step of the unconstrained and zero-constrained inverse solutions are, respectively.

$$\mathbf{R}^k=\left(\boldsymbol{\Gamma}^{k^T}\mathbf{V}^{-1}\boldsymbol{\Gamma}^k+\mathbf{M}\right)^{-1}\boldsymbol{\Gamma}^{k^T}\mathbf{V}^{-1}\boldsymbol{\Gamma}^k \quad (15)$$

and

$$\mathbf{R}^{k'}=\{\mathbf{I}-\left(\boldsymbol{\Gamma}^{k^T}\mathbf{V}^{-1}\boldsymbol{\Gamma}^k+\mathbf{M}\right)^{-1}\mathbf{F}^T\left[\mathbf{F}\left(\boldsymbol{\Gamma}^{k^T}\mathbf{V}^{-1}\boldsymbol{\Gamma}^k+\mathbf{M}\right)^{-1}\mathbf{F}^T\right]^{-1}\mathbf{F}\}\mathbf{R}^k. \quad (16)$$

Using equation (15) or (16), we can compute the resolution matrices for single steps of the sequential inversion. $\mathbf{R}^k$ or $\mathbf{R}^{k'}$, describe the averaging between parameters in the $N+1$ time meshes being estimated. For example, for $N=2$, two data sets are used to estimate difference attenuation at time k, and those estimates may also depend on difference attenuation at times $k-1$ and $k+1$. We can also calculate the resolution matrix for sequential inversion, $\mathbf{R}^k_{seq}$, such that

$$\Delta\hat{\boldsymbol{\alpha}}^k=\mathbf{R}^k_{seq}\begin{bmatrix}\Delta\boldsymbol{\alpha}^{k-1}\\ \Delta\boldsymbol{\alpha}^k\\ \Delta\boldsymbol{\alpha}^{k+1}\end{bmatrix}. \quad (17)$$

The matrix $\mathbf{R}^k_{seq}$ is not square, but *nnodes* by $2(N+1)$ *nnodes*. A row i of $\mathbf{R}^k_{seq}$ describes the influence of parameters in the $k-N+1$ to $k+N-1$ time sets on the estimate of parameter i

in the k-time mesh. $\mathbf{R}^k_{seq}$ is constructed from the rows of $\mathbf{R}^k$ corresponding to the averaging kernels for $\hat{\alpha}^k$. The constrained sequential-estimation resolution matrix is constructed in the same manner from the rows of $\mathbf{R}^{k'}$. It is also possible to derive data resolution matrices for sequential inversion to examine data reproduction for various source-receiver geometries and parameterizations.

EXAMPLES

We demonstrate sequential time-lapse inversion for synthetic examples in which radar tomography is used to monitor a sodium-chloride (NaCl) tracer test. The examples are based loosely on a field experiment conducted at the U.S. Geological Survey Fractured Rock Research Site in New Hampshire (Lane et al., 1998, 2000). Solute transport simulation yields tracer concentrations in the image plane, which are converted into difference-attenuation values. Following a comparison of time-lapse inversion to conventional snapshot inversion, we explore strategies to enhance model resolution by (1) employing different source-receiver geometries in alternating time steps, (2) using different numbers of data sets for sequential estimation, and (3) imposing ray-based inversion constraints to restrict attenuation changes to regions traversed by raypaths that show strong attenuation.

Calculation of synthetic tracer concentrations

We model a doublet tracer test, with continuous injection in well W1 and continuous extraction from well W4 (Figure 2). The NaCl tracer is injected at a concentration of 50 g/liter in a 1.5-m interval in W1, under a flow rate of 3.0×10^{-5} m^3/s. Tracer injection occurs for 10 minutes, after which freshwater is injected at the same rate. The extraction is from a 1.5-m long interval in W4, with a pumping rate of 6.0×10^{-5} m^3/s. Injection and extraction are both at a depth of 25 m below the overburden-bedrock interface, within a 3-m thick fracture zone with a hydraulic conductivity of 5.0×10^{-4} m/s. The hydraulic conductivity of the surrounding bedrock is 1.0×10^{-7} m/s. An effective porosity of 0.001 is assumed, representative of fractured crystalline rock at the site (Shapiro, 1996). We assume longitudinal and transverse dispersivities of 0.50 m and 0.2 m, respectively. Assuming conservative transport, the governing equations are those of 3-D steady-state groundwater flow (18), Darcy's Law (19), and transient advective-dispersive solute transport (20):

$$\frac{\partial}{\partial x_i}\left(K_{ij}\frac{\partial h}{\partial x_j}\right) + Q_s(\mathbf{x}) = 0 \tag{18}$$

$$v_i = -\frac{K_{ij}}{\theta}\frac{\partial h}{\partial x_j} \tag{19}$$

$$\frac{\partial}{\partial x_i}\left(D_{ij}\frac{\partial C}{\partial x_j}\right) - v_i\frac{\partial C}{\partial x_i} + \frac{Q_s(\mathbf{x})}{\theta}(C_s - C) - \frac{\partial C}{\partial t} = 0, \tag{20}$$

where h is hydraulic head, K_{ij} are elements of the hydraulic conductivity tensor, $Q_s(\mathbf{x})$ is the flow rate per unit volume of sources or sinks at spatial location $\mathbf{x}$, x_i is the spatial Cartesian coordinate in direction i, C is concentration, D_{ij} are elements of the dispersion tensor, which is a function of longitudinal and transverse dispersivitities, v_i are the components of average linear pore velocity determined from equations (18) and (19), t is time, C_s is the concentration of the source or sink, and θ is the effective porosity.

Synthetic tracer concentrations were generated using the RKGFE finite-element ground-water flow and solute-transport model (Gandhi et al., 2002). The boundary conditions for flow are zero-drawdown (constant head) at the top of the mesh, corresponding to an interface with high-K overburden material, and zero-gradient (no-flow) boundaries on all other sides. Boundary conditions for transport are zero-flux on all sides, and the initial condition is zero-concentration everywhere. Simulated tracer concentration histories are shown for several locations in Figure 3.

Calculation of synthetic difference-amplitude data

Difference-amplitude data are generated for cross-hole surveys in the W2–W3 plane. Lane et al. (2000) developed a formula to relate changes in radar attenuation to changes in NaCl concentration by combining an effective-medium model of attenuation as a function of fluid conductivity with tabulated

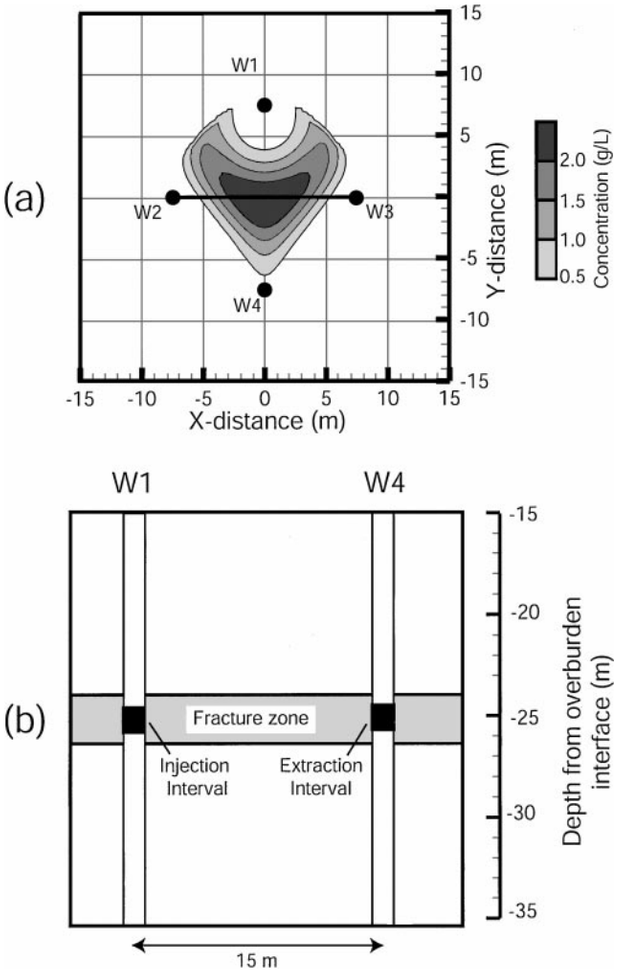

FIG. 2. (a) Doublet tracer-test design, plan view with tracer plume concentrations at 100 minutes in the $Z = -25$ m plane, and (b) cross-sectional view between wells W1 and W4. Synthetic cross-hole data are generated for the W2–W3 plane.

values of conductivity for NaCl solutions of different concentration. Using their approach, we find a regression equation to predict difference attenuation from concentration for an effective porosity of 0.001. Third-order polynomial regression yields

$$\Delta\alpha = 0.226C - 1.5 \times 10^{-3}C^2 + 7 \times 10^{-6}C^3, \qquad (21)$$

where difference-attenuation is in decibels/meter, concentration is in grams/liter, and the regression is constrained to predict zero difference attenuation for a concentration of 0 g/liter. Using equation (21), nodal concentration values are converted to difference attenuation. Radar difference-amplitude data are then calculated using equation (5).

Setup of inversion examples

In all inversion examples, each time-set of data is collected over a 10-minute window and includes difference-amplitude measurements for 328 raypaths. Common-source gathers are collected from four evenly spaced points in each well (Figure 4). Measurements are made at receiver locations in spatial increments of 0.5 m and time increments divided evenly over the 10-minute window. The inversion parameters are nodal difference-attenuation values on a time series of 2-D (x, z) meshes. The composite 3-D (x, z, t) mesh has a 10-minute temporal spacing, and 0.6-m x- and z-spacing, for a total of 825 nodes in each 2-D mesh. The same inversion parameters are used for all configurations (Table 1). The mean is assumed to be spatially uniform, but takes a different value in each time mesh. Ideally, different data variances, model-parameter correlation ranges, and model-parameter variances should be used in different time steps. In practice, these parameters would be unknown and selected based on initial results.

In generating synthetic difference-amplitude data, we assume normally distributed measurement errors with a mean of zero and standard deviation of 0.02 dB, which is approximately 5% of the mean difference-amplitude for the data set analyzed. Error management is important for difference tomography in general and attenuation tomography specifically (Holliger et al., 2001), but it is not a major focus of this study. Rather, our goal is to present and demonstrate a space-time parameterization and inversion method. Methods for handling data error include (1) pre-inversion data processing, (2) data weighting schemes, and (3) use of appropriate regularization to produce smooth or damped tomograms less affected by data errors. The interested reader is referred to Peterson (2001) for a recent review of pre-inversion data processing and correction for radar tomography, and to Holliger et al. (2001) for insight into the limitations of ray-based amplitude tomography. It should be noted that the approach presented here is compatible with pre-inversion data correction and that it could be extended to include alternative measures of misfit (e.g., the L_1 norm) less prone than least-squares to data error (e.g., Claerbout and Muir, 1973).

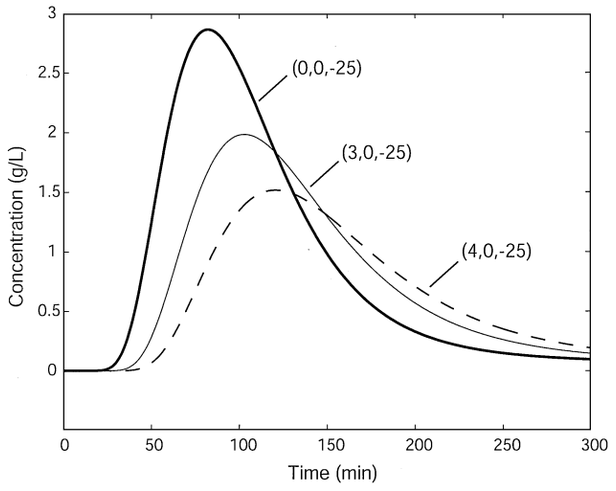

FIG. 3. Tracer concentration histories at several points in the image plane.

Inversion results for the five examples are compared in Figure 5, which include images of the true difference attenuation, the estimated difference attenuation, and the estimation error, defined as the true minus the predicted difference attenuation. For display, results are interpolated to a finer mesh with a 0.3-m discretization according to the same interpolation scheme used to build the forward model. Note that this is consistent with our parameterization and forward model; it does not artificially refine or smooth the results. Table 2 reports the mean squared error (MSE) between synthetic and estimated model parameters, and the MSE between synthetic and predicted difference-amplitude data for each example. These error measures are computed for the tomograms shown in Figure 5.

Comparison of time-lapse and snapshot inversion

The first two inversion examples compare our time-lapse inversion to conventional snapshot tomography. In example 1, snapshot inversion is used to generate each tomogram from a single difference-amplitude data set, neglecting measurement time. The source-receiver geometry for example 1 is shown in Figure 4a. Snapshot tomograms will best approximate difference attenuation in the middle of the time-step in which data are collected. Thus, inversion of data collected between 50 and 60 minutes yields estimates of difference attenuation at 55 minutes.

Artifacts are apparent in the inverted 55-minute snapshot tomogram (Figure 5a). The magnitude of estimation error varies over the tomogram and is not symmetric, because of the nonuniform error in assumed data-collection time. Data collected early in the scan reflect an anomaly of one size and magnitude, whereas data collected later in the scan see the anomaly at a different size and magnitude. Inconsistencies between data collected at different times result in tomograms with nonsymmetric streaks and negative values, where the inversion attempts to compensate for neglected temporal variation by

Table 1. Parameter values used for inversion of synthetic data.

Inversion parameter	Assumed value
Standard measurement error	0.02 dB
Temporal range	40 minutes
Spatial range	5 m
Model variance	0.01 dB^2/m^2

generating spurious spatial variation. Consequently, snapshot inversion could lead to misinterpretation of the path of tracer migration, as well as the timing of the peak concentration in the image plane.

In inversion example 2, we use time-lapse inversion with the same source-receiver geometry (Figure 4b), discretization, and inversion parameters used in example 1. The time-lapse inversion uses two time-sets of data to estimate each time-set of nodal difference-attenuation values. Each step of the inversion involves estimation of difference attenuation at 2475 nodes based on 656 difference-amplitude data. Although the number of estimated parameters is triple that of

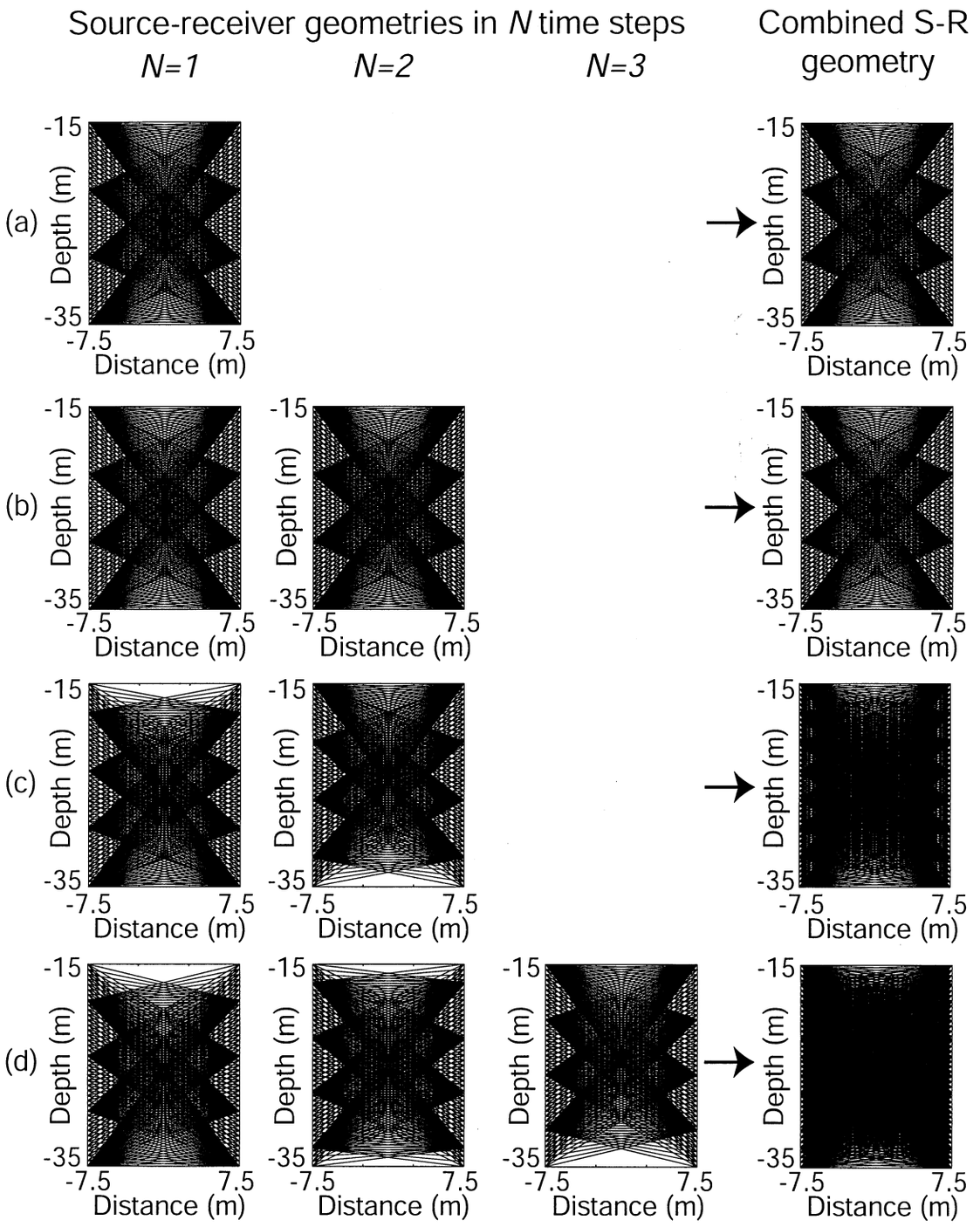

FIG. 4. Source-receiver geometries for (a) example 1, (b) examples 2 and 5, (c) example 3, and (d) example 4. In (c) and (d), different data are collected in different time steps and used jointly for inversion. Borehole W2 is located along the left side of each ray plot, and borehole W3 is located along the right.

example 1, the quality of the inversion is dramatically improved (Figure 5b). The MSE of estimation decreases by 90% from 1.4×10^{-4} to 1.5×10^{-5} dB^2/m^2, and error is more uniform across the tomogram. Streak artifacts present in the snapshot tomograms of example 1 do not appear in tomograms generated using sequential time-lapse inversion. Time-lapse inversion also improves the match to the data. The mean-squared data residual is also reduced by an order of magnitude (Table 2).

Resolution enhancement through time-lapse inversion

The time-lapse inversion framework facilitates a number of experimental and mathematical strategies to improve model resolution and thereby enable more robust interpretation of tomograms. In this section, we explore resolution enhancement through (1) survey-design modification to include different raypaths in alternating time steps, (2) consideration of three data sets to estimate each time-set of difference

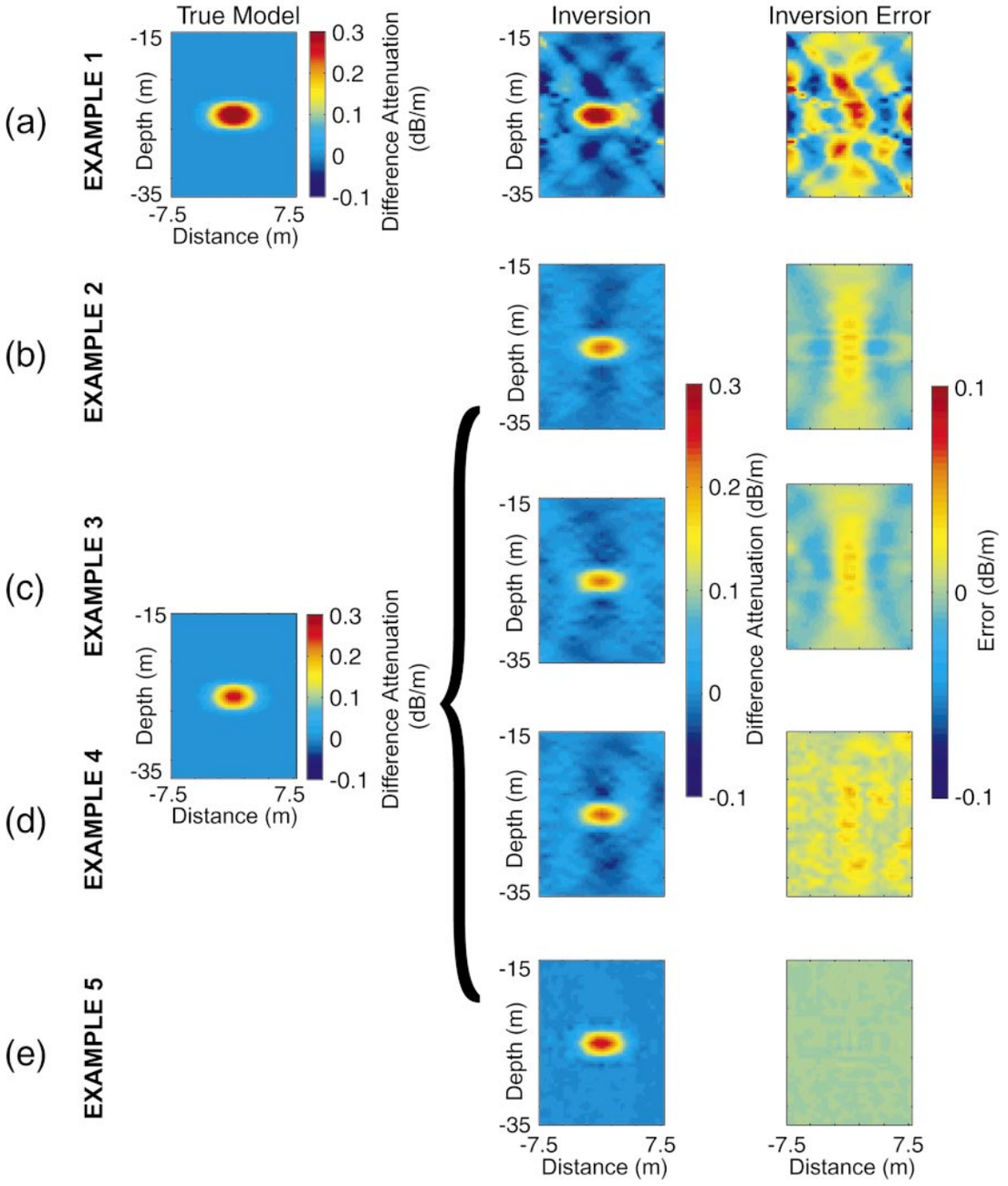

FIG. 5. Inversion results for examples 1 to 5. Column 1 shows the true difference-attenuation in the W1–W2 plane at time 55 minutes (a) and 50 minutes (b–e) in decibels/meter. Column 2 shows inverted tomograms. Column 3 shows the estimation error, the difference between images in columns 1 and 2.

attenuation, and (3) application of ray-based constraints to focus difference-attenuation anomalies.

Insight into the nonsymmetric streak artifacts apparent in the snapshot tomograms of example 1 can be gained by examining the resolution matrices for the inversion, which reveal the dependence of difference-attenuation estimates on true difference attenuation at times k and $k+1$. The diagonals of these matrices (Figures 6a, b) show that some estimates are controlled by difference-attenuation values at the earlier time, others are controlled by values at the later time. Hence, resolution varies spatially within the tomogram, and the streak artifacts in Figure 5a result from averaging across time as well as space.

The diagonal of the resolution matrix, $\mathbf{R}^k_{seq}$, for time-lapse inversion example 2 is shown in Figure 6c. The image is nearly symmetric, in contrast to Figure 6a. Consideration of staggered measurement time and the use of space-time parameterization suppress the streak artifacts observed in snapshot tomograms. The resolution matrices for Examples 1 and 2 provide the basis for evaluating the benefits of resolution-enhancement strategies.

Effect of alternating raypath geometry: Example 3.—In example 3, two different source-receiver geometries are used in alternating time steps (Figure 4c) in an effort to capitalize on space-time correlation of difference attenuation. This scenario includes the same number of rays as the two previous, and employs the same inversion parameters. Collection of different rays in alternating time steps improves model resolution over much of the image plane (Figure 6d). The inverted tomograms are similar to results from example 2, in which one raypath geometry was repeated. The MSE of overall prediction error is the same as for example 2, but the MSE between observed and predicted data improves from 9.3×10^{-5} to 3.1×10^{-5} dB^2 (Table 2). Model resolution and data reproduction are improved by use of alternating source-receiver geometries, without loss of estimation accuracy.

Effect of inversion using additional time-sets of data: Example 4.—In this scenario, we evaluate the effect of incorporating an additional time-set of data ($N = 3$) in each estimation step. We sequentially estimate four time sets of difference-attenuation parameters from three time-sets of data, using a single, repeated source-receiver geometry (Figure 4d). Consideration of the additional data appears to improve model resolution in parts of the image plane (Figure 6e), but the

Table 2. Computed mean absolute deviations for parameter estimates (estimated versus true) and data residuals (simulated versus observed).

Example	Mean squared estimation error (dB^2/m^2)	Mean squared data residual (dB^2)
1	1.4×10^{-3}	1.3×10^{-3}
2	1.5×10^{-4}	9.3×10^{-5}
3	1.5×10^{-4}	3.1×10^{-5}
4	2.2×10^{-4}	3.1×10^{-4}
5	6.0×10^{-6}	3.7×10^{-5}

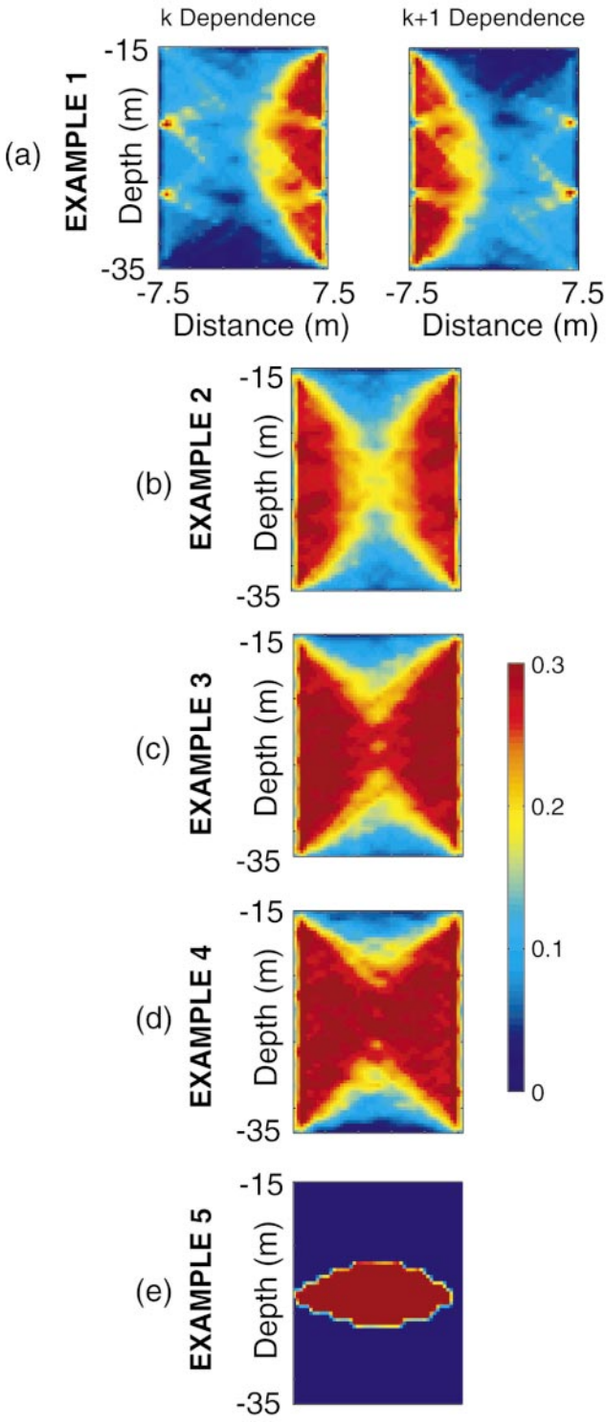

FIG. 6. Diagonal elements of resolutions matrices for (a) snapshot inversion, (b) time-lapse inversion using a single source-receiver geometry, (c) time-lapse inversion using two source-receiver geometries in alternating time steps, and (d) time-lapse inversion using three source-receiver geometries, and (e) time-lapse inversion using two source-receiver geometries and ray-based constraints.

estimation error and data reproduction are degraded compared to examples 2 and 3 (Table 2). The size, shape, and magnitude of the anomaly are changing too quickly to use three data sets to advantage for the problem considered. This finding supports the application of time-lapse inversion using only a limited number of time-sets of data. Use of data from multiple times may improve or degrade inversion results depending on the assumed space-time covariance model, the spatiotemporal mean, the true rate of change of parameter values, and the magnitude of data error. However, the inversion results for example 4 are still far superior to results from snapshot inversion.

Effect of imposing ray-based constraints: Example 5.—As in the third example, two different source-receiver geometries are used in alternating time steps ($N = 2$) (Figure 4c). In addition, linear constraints restrict changes in attenuation to only those regions of the tomogram traversed by raypaths corresponding to large difference-amplitude data. In this example, we determine the low difference-amplitude rays as those that correspond to the 40th percentile of the difference-amplitude measurements. Nodes with more than 5% of their ray density attributed to low difference-amplitude rays were constrained to zero-difference attenuation in the inversion.

Application of ray-based constraints greatly reduces estimation error (Figure 5e) and improves model resolution in the vicinity of the difference-attenuation anomaly (Figure 6f) at the expense of resolving parameters at the zero-constrained nodes. Compared to results from example 3, which considered the same source-receiver geometry, the constrained inversion results in lower estimation error. As expected, the constrained inversion produces a larger data misfit (Table 2). Despite the addition of constraints, data reproduction remains superior to snapshot inversion, owing to the use of space-time parameterization and consideration of attenuation change during data acquisition.

In establishing constraints, selection of cutoffs should be guided by the results of initial, unconstrained inversions and by plots of the raypaths corresponding to high and low difference-amplitude data. If the target anomaly changes significantly in size, location or shape, care must be exercised in applying constraints. Plots of high and low difference-amplitude rays should be examined for each time-lapse data set.

CONCLUSIONS

The combination of time-lapse geophysical monitoring and conventional hydrogeologic tests provides more detailed aquifer characterization than heretofore possible. Geophysical monitoring of fluid flow or solute transport may provide valuable calibration data for hydrogeologic models. However, in cases where the target feature varies more quickly than the data collection process, accurate tomographic inversion must account for temporal variations in the imaged physical properties. Toward this end, we presented a sequential-inversion approach to time-lapse radar tomography based on a forward model that accounts for precise data collection times and a parameterization that allows for temporal regularization. A synthetic example demonstrated the benefit of sequential time-lapse inversion over the conventional snapshot approach. Snapshot tomograms contained large errors and streak artifacts that would complicate interpretation. Time-lapse inversion resulted in reduced estimation error, improved model resolution, and superior data reproduction.

We presented formulas to compute the model resolution matrices for the unconstrained and constrained versions of our sequential time-lapse inversion method to provide tools to evaluate the benefit of alternative data configurations, regularization, and constraints on inversion results. Through synthetic examples, we explored simple strategies to further improve model resolution by exploiting temporal correlation. This is achieved by collecting data for different raypaths in alternating time steps and by inverting data jointly in space and time. The use of ray-based constraints enhances model resolution by limiting attenuation changes to regions of the tomogram traversed by high difference-amplitude rays.

Space-time parameterization and sequential-inversion were demonstrated for linear, difference-attenuation tomography. The approach could also be applied to other linear, tomographic problems and could be extended to solve nonlinear problems in an iterative manner. Analysis of time-lapse data using other inverse methods, such as SIRT or RAYPT, may also benefit from the use of space-time parameterization and regularization.

ACKNOWLEDGMENTS

We gratefully acknowledge support provided by the National Science Foundation through research and equipment grants numbered EAR-9705812 and EAR-9707031 awarded to S. M. Gorelick, and support provided by the EPA STAR Fellowship Program through Fellowship U-915155-01-0 awarded to F. D. Day-Lewis. We thank John W. Lane, Jr. for his insights into cross-hole radar survey design and experimental procedures, and for useful discussions regarding tomographic resolution. We are grateful to Rahul K. Gandhi for use of the groundwater flow and solute transport model used in this study, and to Joel E. VanderKwaak for use of the WatSolv sparse matrix iterative solver used by the model (VanderKwaak, 1997). We thank David Boerner, Andrew Curtis, and the anonymous reviewer for their helpful comments regarding this work.

REFERENCES

Archie, G. E., 1942, The electrical resistivity log as an aid in determining some reservoir characteristics: Trans. Am. Inst. Min., Metall., Petr. Eng., **146**, 54–62.

Brewster, M. L., and Annan, A. P., 1994, Ground-penetrating radar monitoring of a controlled DNAPL release: 200 MHz radar: Geophysics, **59**, 1211–1221.

Brewster, M. L., Annan, A. P., Greenhouse, J. P., Kueper, B. H., Olhoeft, G. R., Redman, J. D., and Sander, K. A., 1995, Observed migration of a controlled DNAPL release by geophysical methods: Ground Water, **33**, 977–987.

Censor, Y., 1983, Finite series-expansion reconstruction methods: Proc. IEEE, **71**, 409–419.

Claerbout, J. F., and Muir, F., 1973, Robust modeling with erratic data: Geophysics, **38**, 826–844.

Copty, N., Rubin, Y., and Mavko, G., 1993, Geophysical-hydrogeological identification of field permeabilities through Bayesian updating: Water Resources Research, **29**, 2813–2825.

Eppstein, M. J., and Dougherty, D. E., 1998a, Efficient three-dimensional data inversion: Soil characterization and moisture monitoring from cross-well ground-penetrating radar at a Vermont test site: Water Resources Research, **34**, 1889–1900.

——— 1998b, Optimal 3-D traveltime tomography: Geophysics, **63**, 1053–1061.
Ezzedine, S., Rubin, Y., and Chen, J., 1999, Hydrological-geophysical Bayesian method for subsurface site characterization: Theory and application to LLNL Superfund Site: Water Resources Research, **35**, 2671–2684.
Gandhi, R. K., Hopkins, G. D., Goltz, M. N., Gorelick, S. M., and McCarty, P. L., 2002, Fullscale demonstration of in-situ cometabolic biodegradation of trichloroethylene in groundwater, 1: Dynamics of a recirculating well system: Water Resources Research, **38**, 9-1–9-6.
Holliger, K., Musil, M., and Maurer, H. R., 2001, Ray-based amplitude tomography for crosshole georadar data: A numerical assessment: J. Appl. Geophys., **47**, 285–298.
Hubbard, S. S., Chen, J., Peterson, J., Majer, E. L., Williams, K. H., Swift, D. J., Mailloux, B., and Rubin, Y., 2001, Hydrogeological characterization of the South Oyster Bacterial Transport Site using geophysical data: Water Resources Research, **37**, 2431–2456.
Hubbard, S., Rubin, Y., and Majer, E., 1999, Spatial correlation structure estimations using geophysical data: Water Resources Research, **35**, 1809–1825.
Hyndman, D. W., and Gorelick, S. M., 1996, Estimating lithologic and transport properties in three dimensions using seismic and tracer data: The Kesterson Aquifer: Water Resources Research, **32**, 2659–2670.
Hyndman, D. W., and Harris, J. M., 1996, Traveltime inversion for the geometry of aquifer lithologies: Geophysics, **61**, 1728–1737.
Hyndman, D. W., Harris, J. M., and Gorelick, S. M., 1994, Coupled seismic and tracer test inversion for aquifer property characterization: Water Resources Research, **30**, 1965–1977.
——— 2000, Inferring the relation between seismic slowness and hydraulic conductivity in heterogeneous aquifers: Water Resources Research, **36**, 2121–2132.
Istok, J., 1989, Groundwater modeling by the finite element method: Am. Geophys. Union.
Kitanidis, P. K., 1995, Quasi-linear geostatistical theory for inversing: Water Resources Research, **31**, 2411–2419.
——— 1996, On the geostatistical approach to the inverse problem: Advances in Water Resources, **19**, 333–342.
Kitanidis, P. K., and Vomvoris, E. G., 1983, A geostatistical approach to the inverse problem in groundwater modeling (steady state) and one-dimensional simulations: Water Resources Research, **19**, 677–690.
Kyriakidis, P. C., 1999, Stochastic simulation of spatiotemporal phenomenon: Ph.D. Thesis, Stanford Univ.
Lane, J. W., Jr., Day-Lewis, F. D., Harris, J. M., Haeni, F. P., and Gorelick, S. M., 2000, Attenuation-difference radar tomography: Results of a multiple-plane experiment at the U.S. Geological Survey Fractured Rock Research Site, Mirror Lake, New Hampshire: Proc. Eighth Internat. Conf. Ground Penetrating Radar, 666–675.
Lane, J. W., Jr., Haeni, F. P., and Day-Lewis, F. D., 1998, Use of time-lapse attenuation-difference radar tomography methods to monitor saline tracer transport in fractured crystalline bedrock: Proc. Seventh Internat. Conf. Ground Penetrating Radar, 533–538.
Marion, D. A., Nur, A., Yin, H., and Han, D., 1992, Compressional velocity and porosity in sand-clay mixtures: Geophysics, **57**, 554–563.
Maurer, H., Holliger, K., and Boerner, D. E., 1998, Stochastic regularization: Smoothness or similarity?: Geophys. Res. Lett., **25**, 2889–2892.
Menke, W., 1989, Geophysical data analysis: Discrete inverse theory, rev. ed.: Academic Press.
Michelena, R., and Harris, J. M., 1991, Tomographic traveltime inversion using natural pixels: Geophysics, **56**, 635–644.
Olsson, O., Anderson, P., and Gustafsson, E., 1991, Site characterization and validation-monitoring of saline tracer transport by borehole radar measurements: Swedish Nuclear Fuel and Waste Management Co. Final Report Stripa Project TR91-18.
Olsson, O., Falk, L., Forslund, O., Lundmark, L., and Sandberg, E., 1992, Borehole radar applied to the characterization of hydraulically conductive fracture zones in crystalline rock: Geophys. Prosp., **40**, 109–142.
Osiensky, J. L., and Donaldson, P. R., 1995, Electrical flow through an aquifer for contaminant source leak detection and delineation of plume evolution: J. Hydrology, **169**, 243–263.
Peterson, J. E., Jr., 2001, Pre-inversion corrections and analysis of radar tomographic data: J. Environ. Eng. Geophys., **6**, 1–18.
Peterson, J. E., Paulsson, B. N. P., and McEvilly, T. V., 1985, Application of algebraic reconstruction techniques to crosshole seismic data: Geophysics, **50**, 1556–1580.
Poeter, E., Wingle, W. L., and McKenna, S. A., 1997, Improving groundwater project analysis with geophysical data: The Leading Edge, **16**, 1075–1681.
Ramirez, A., Daily, W., Binley, A. M., LaBrecque, A., and Roelant, D., 1996, Detection of leaks in underground storage tanks using electrical resistance methods: J. Environ. Eng. Geophys., **1**, 189–203.
Rouhani, S., and Myers, D. E., 1990, Problems in spatiotemporal kriging of geohydrological data: Mathematical Geology, **22**, 611–623.
Rubin, Y., Mavko, G., and Harris, J., 1992, Mapping permeability in heterogeneous aquifers using hydrological and seismic data: Water Resources Research, **28**, 1192–1800.
Shapiro, A. M., 1996, Estimation of effective porosity in fractured crystalline rock by controlled-tracer tests: Joint U.S. Geological Survey, U.S. Nuclear Regulatory Commission Workshop on Research Related to Low-level Radioactive Waste Disposal, 185–190.
Singh, R. P., and Singh, Y. P., 1991, RAYPT: A new inversion technique for geotomographic data: Geophysics, **56**, 1215–1227.
Slater, L., Binley, A. M., Daily, W., and Johnson, R., 2000, Cross-hole electrical imaging of a controlled saline tracer injection: J. Appl. Geophys., **44**, 85–102.
Slater, L. D., and Sandberg, S. K., 2000, Resistivity and induced polarization monitoring of salt transport under natural hydraulic gradients: Geophysics, **65**, 408–420.
Stratton, J. A., 1941, Electromagnetic theory: McGraw-Hill Book Co.
VanderKwaak, J. E., Forsyth, P. A., MacQuarrie, K. T. B., and Sudicky, E. A., 1987, WatSolv sparse matrix iterative solver user's guide for version 2.16: Univ. of Waterloo.
Vasco, D. W., Datta-Gupta, A., and Long, J. C. S., 1997, Resolution and uncertainty in hydrologic characterization: Water Resources Research, **33**, 379–397.
Vesnaver, A., and Böhm, G., 1999, In quest of the grid: Geophysics, **64**, 1116–1125.
——— G., 2000, Staggered or adapted grids for seismic tomography: The Leading Edge, **19**, 944–950.
White, P. A., 1988, Measurement of ground-water parameters using salt-water injection and surface resistivity: Ground Water, **26**, 179–186.

APPENDIX

SPACE-TIME INTERPOLATION FUNCTIONS

The value of the interpolation function, w_j^k, for node j in time-mesh k is equal to one at that node, zero in elements not containing the node, and zero at all other nodes. Calculation of the interpolation function values is performed in a local coordinate system. An element can have arbitrary dimensions in the global $(\mathbf{x}, t)$ coordinate system, but is mapped to a $2 \times 2 \times 2$ cube with local coordinate system $(\varepsilon, \eta, \zeta)$, in which ε, η and ζ each range from -1 to 1 across the element (Figure A-1). In the local system, the interpolation function at a point is

$$w_j^k(\varepsilon, \eta, \varsigma) = \frac{1}{8}(1 + \varepsilon\varepsilon_j)(1 + \eta\eta_j)(1 + \varsigma\varsigma^k), \quad \text{(A-1)}$$

where $w_j^k(\varepsilon, \eta, \varsigma)$ is the interpolation function of node j in the k mesh at local space-time location $(\varepsilon, \eta, \zeta)$, and ε_j, η_j, ζ^k are the local coordinates of node j in the k-time mesh.

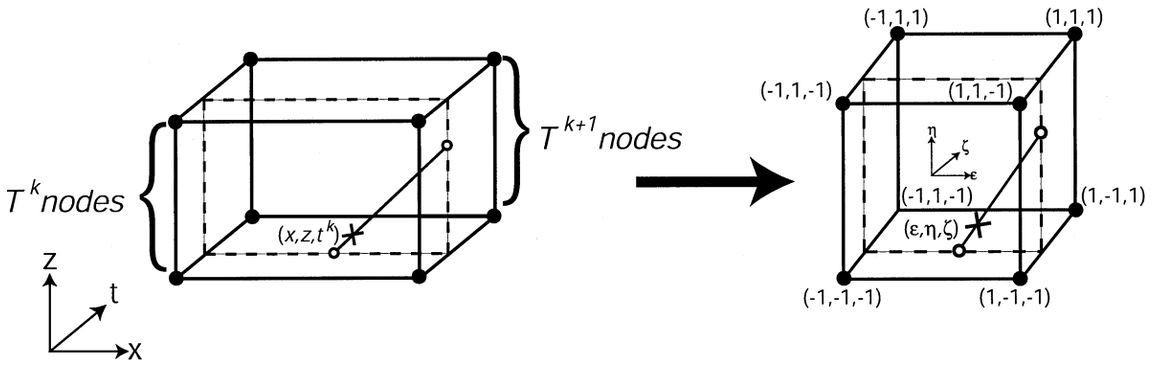

FIG. A-1. Interpolation in parametric cubic quadrilateral elements.